Facile synthesis and characterization of anatase TiO_2/g-CN composites for enhanced photoactivity under UV-visible spectrum

Sayed Mukit Hossain [1], Heeju Park [2], Hui-Ju Kang [3], Jong Seok Mun [3], Leonard Tijing [1], Inkyu Rhee [4], Jong-Ho Kim [2,*], Young-Si Jun [3,*] and Ho Kyong Shon [1,*]

[1] Faculty of Engineering and IT, University of Technology, Sydney, P.O. Box 123, Broadway, NSW 2007, Australia; sayed.m.hossain@student.uts.edu.au (S.M.H.); leonard.tijing@uts.edu.au (L.T.); Hokyong.Shon-1@uts.edu.au (H.K.S.)

[2] School of Chemical Engineering, Chonnam National University, Gwangju 61186, Korea; point1014@hanmail.net (H.P.); answhdtjr8726@gmail.com (J.S.M.); jonghkim@chonnam.ac.kr (J.-H.K)

[3] Department of Advanced Chemicals & Engineering, Chonnam National University, 77 Yongbong-ro, Buck-gu, Gwangju 61186, Republic of Korea; gmlwn120@gmail.com (H.-J.K.); youngsi.jun@gmail.com (Y.-S.J)

[4] Department of Civil Engineering, Chonnam National University, Gwangju 61186, Korea; rheei@chonnam.ac.kr (I.R.)

* Correspondence: Hokyong.Shon-1@uts.edu.au (H.K.S.); youngsi.jun@gmail.com (Y.S.J); Tel.: +61 447 332 707 (H.K.S.)

Abstract

For the purpose of atmospheric NO removal, anatase TiO_2/g-CN photocatalytic composites were prepared by using a facile template-free calcination route in atmospheric conditions. Considerably fiscal NP400 and laboratory-grade melamine were used as the precursor of the composites. Additionally, samples were prepared with different wt. ratios of TiO_2 and melamine by using two distinct calcination temperatures (550°C/600°C). The morphological attributes of the composites were assessed with X-ray diffraction, scanning and transmission electron microscopy, infrared spectroscopy, and X-ray photoelectron spectroscopy. Additionally, the optical traits were evaluated and compared using UV-visible diffuse reflectance spectroscopy and photoluminescence analysis. Finally, the photodegradation

potentials for atmospheric NO by using the as-prepared composites were assessed under both UV and visible light irradiation. All the composites showed superior NO oxidation compared to NP400 and bulk g-CN. For the composites prepared by using the calcination temperature of 550°C, the maximum NO removal was observed when the NP400 to melamine ratio was 1:2, irrespective of the utilized light irradiation type. Whereas for increased calcination temperature (600°C), the maximum NO removal was observed at the precursor mix ratio of 1:3 (NP400:melamine). Successfully narrowed energy bandgaps were perceived in the as-prepared composites. Moreover, a subsequent drop in NO_2 generation during NO oxidation was observed under both UV and visible light irradiation. Interestingly, higher calcination temperature during the synthesis of the catalysts has shown a significant drop in NO_2 generation during the photodegradation of NO.

Keywords

NO_x removal, TiO_2/g-CN, Photooxidation, Nitrate selectivity, UV-Vis activation, NO_2 generation

1 Introduction

Atmospheric pollution caused by nitrogen oxides (NO_x) has been identified as one of the most severe environmental problems (Song et al., 2019; Yang et al., 2019). Usually, NO_x refers to NO and NO_2, the two most common atmospheric nitrogen oxides. Anthropogenic activities such as combustion-based emission of natural gases and denitrification of nitrate salts from biogenic sources are the primary cause of atmospheric NO_x (Schwartz-Narbonne et al., 2019). Over the past decades, NO_x concentration has acutely increased, leading to dense haze events by generating secondary aerosols. Researchers have demonstrated effective removal of gaseous NO_x using several physio-chemical processes such as direct decomposition (Damma et al., 2018), selective catalytic/non-catalytic reduction (Zong et al., 2018), solid-liquid adsorption (Mamaghani et al., 2017), plasma-assisted catalytic reduction (Oskooei et al., 2019), and photocatalytic oxidation. However, most of these approaches are only useful at the source of emission where the NO_x concentration is at ppm levels and requires specific tools, tuning, or high temperatures. Photocatalytic oxidation is very efficient in removing NO_x at the ppb level in ambient atmospheric conditions (Tsang et al., 2019). Moreover, photocatalytic NO_x oxidation facilitates sustainability by utilizing renewable solar energy, mild reaction conditions, low cost, and large-scale

implementation (Schwartz-Narbonne et al., 2019; Yang et al., 2019). This promising method can effectively oxidize NO_x by generating reactive oxygen species such as superoxide ($^{\cdot}O_2^-$) or hydroxyl ($^{\cdot}OH$) radicals under light irradiation (Martinez-Oviedo et al., 2019).

Since the TiO_2 electrode was implemented for H_2 evolution using solar irradiation by Fujishima and Honda, it gained a growing interest in photocatalysis (Wei et al., 2016). The low cost, chemical stability, and non-toxic nature of TiO_2 made it an ideal photocatalyst (Tsang et al., 2019). Moreover, theoretical and experimental studies indicated that the dominant anatase facets ((101), (001)) of TiO_2 are more photoactive compared to the dominant rutile facets (Huang et al., 2018). However, the photocatalytic activities of anatase TiO_2 are limited by its large energy bandgap (~3.6 eV) and prompt recombination of photogenerated e^-/h^+ pairs (Huang et al., 2020). Consequently, conventional TiO2 primarily works under UV illumination, having a wavelength below 387 nm, with a low quantum efficiency. Hence, during photocatalysis, TiO_2 can only utilize a maximum of 4% – 5% of the solar spectrum (Huang et al., 2020), most of which is wasted by recombination in the bulk phase. For decades, many attempts have been made to enhance the photoactivity of TiO_2 by employing a more substantial portion of the solar spectrum and well-defined structure with high crystallinity through bandgap and crystal engineering (Lu et al., 2010; Yan and Yang, 2011), respectively. Some of the successful techniques that have been found are sol-gel method combined with inorganic/organic templates (Pan et al., 2011; deKrafft et al., 2012), hydrothermal synthesis (Yu et al., 2013a), surface sensitization, metal/non-metal doping, noble metal deposition, self-doping, and semiconductor heterojunction (Zhang et al., 2019a; Zhang et al., 2019c). In particular, the heterojunction of TiO_2 with restricted bandgap semiconductors is very efficient in utilizing the visible and solar light spectrum as well as mitigating charge recombination during photocatalysis.

In recent years, polymeric derivative (g-CN) of ideal graphitic carbon nitride or polymeric melon have attracted considerable attention due to their promising optical properties, electronic structure, and photocatalytic behaviour (Thomas et al., 2008; Dong et al., 2011; Dong et al., 2013). g-CN has been significant in working towards photocatalytic H_2 evolution. g-CN can easily be synthesized by thermal polycondensation of a nitrogen-rich molecular precursor such as urea, cyanamide, dicyandiamide,

melamine, and thiourea (Dong et al., 2011). Two basic tectonic units, tri-s-triazine (C_6N_7) and s-triazine (C_3N_3), each provide for the specific architecture of g-CN (Thomas et al., 2008). However, g-CN with standard C_6N_7 units has been predicted to be the most stable phase in low energy conditions (Thomas et al., 2008). Unlike TiO_2, g-CN features a two-dimensional (2D) lamellar structure consisting primarily of the π-conjugated heterocyclic aromatic compounds with a modest energy gap (~2.7 eV), leading to high thermo-chemical stability, strong visible light absorption (~450 – 460 nm), and favourable optoelectronic properties (Zhou et al., 2019; Cui et al., 2020). g-CN has the conduction band (CB) and valence band (VB) potential of −1.3 or +1.4 eV vs. normal hydrogen electrode (NHE) respectively; thus, the photoexcited e^-/h^+ pairs can be efficiently utilized for H_2O splitting (H_2 evolution), organic pollutants degradation, and CO_2 reduction (Zhang et al., 2019a).

Thanks to its impressive π-conjugated structure and visible light absorption, g-CN has drawn tremendous attention to the removal of NO_x, one of the prominent haze precursors (Ma et al., 2016; Li et al., 2018; Wang et al., 2018). Similar to TiO_2, the photocatalytic activities of g-CN is still limited because of the low charge transfer efficiency and high recombination (i.e., the transfer of photogenerated e^- from CB to VB, to combine with photogenerated h^+) rate of the photogenerated e^-/h^+ pairs (Yu et al., 2020). Therefore, the pristine g-CN cannot effectively eliminate NO_x unless modified to inhibit the charge recombination rate and enhance charge transfer efficiency. Hence, to improve photoactivity, substantial attempts have been made for the morphology and energy bandgap amendment of the pristine g-CN. Heteroatom doping and composite preparation with compatible semiconductors through heterojunction are the prominent approaches that have been tested by many research groups. Considering the stability and the extent of the photoactivity of g-CN composites, g-CN heterojunction with other semiconductors appears to be an efficient strategy to optimize photoactivity (Cui et al., 2020; Huang et al., 2020; Yu et al., 2020). The disparity in the CB and VB levels of g-CN and TiO_2, along with the graphene-like 2D structure of g-CN, favours efficient heterojunction, which facilitates dynamic photoactivity under both UV and visible irradiation (Xia et al., 2019; Cui et al., 2020; Huang et al., 2020). Due to the position of CB and VB, TiO_2/g-CN is a type II heterostructure. Therefore, photogenerated e^- on the CB of g-CN can transfer to TiO_2, and the photogenerated h^+ from VB of TiO_2

can transmit to g-CN (Cui et al., 2020). Consequently, the recombination rate of photogenerated e^- and h^+ can be reduced in the TiO_2/g-CN composite. In contrast, several studies reported TiO_2/g-CN to be a type Z heterostructure (Huang et al., 2020).

Although TiO_2/g-CN composites were considered efficient photocatalysts for NO removal, little progress has been made in eliminating the discharged NO_2. While direct NO_2 oxidation generates harmless nitrates, NO oxidation involves several intermediate steps before it is fully oxidized, most involving NO_2 formation. Since NO_2 is more toxic than NO, its release hampers the overall photocatalytic efficiency. Only a selective photocatalyst that suppresses the formation and release of undesired intermediates can ensure improvement in air quality. Additionally, many studies have been conducted on the preparation of TiO_2/g-CN for enhanced photoactivity under visible light (Cui et al., 2020; Huang et al., 2020). Still, the enhancement under UV irradiation was rarely reported (primarily for NO oxidation). Hence, for the outdoor application, it is also essential to assess the behaviour under UV irradiation that boosts the photoactivity of most of wide-and-medium-bandgap semiconductors, including TiO_2 and g-CN. Therefore, in this work, a facile template-free route was utilized to successfully prepare TiO_2/g-CN composites by using NP400 and melamine as the precursors. NP400 is an anatase form of TiO_2, which is prepared by calcining $Ti(OH)_4$ (hydrolyzed product of Ti-based salts) at a temperature of 600°C for 4 – 5 h (Rhee et al., 2018). Therefore, from commercial points of view, it is very low-priced but equally photoactive as commercially available P25. Detailed characterizations of the as-prepared composites were performed, and the NO oxidation potentials of the as-prepared composites were assessed by following ISO 22197-1 (2007) and ISO 17198-1 (2018) for UV and visible light photo-oxidation. Moreover, the nitrate selectivity and possible oxidation scheme were discussed concerning the varying synthesis temperature of the prepared composites.

2 Materials and methods

2.1 Materials

As a precursor of anatase titania, NP400 was provided by Bentech Frontier Co. Ltd. (Gwangju, South Korea). Melamine ($C_3H_6N_6$) in powder form (assay, 99%) was purchased from Sigma-Aldrich Korea (Seoul, South Korea). All the reagents were used directly without further processing.

2.2 Preparation of TiO_2/g-C_3N_4 composite

The heterojunction of TiO_2 and g-CN was achieved by annealing the dry mixture of NP400 (anatase TiO_2, Bentech Frontier) and melamine (Sigma-Aldrich, 99%) in a laboratory scale box furnace under air. Composites were prepared by varying the wt% of melamine (50–500%) compared to NP400, and two sets of calcination temperature (550°C and 600°C) were utilized. The rate of rise of temperature in the box furnace and the duration of calcination were fixed as 10 °C/min and 3 h, respectively. The nomenclature of the prepared samples indicating the varying mixing ratio of the precursors and calcination temperature are illustrated in Table S1. Initially, 6 samples were prepared by calcining the precursor mix of NP400 and melamine at 550°C. The amount of NP400 in the precursor mix was kept fixed at 4 g and the melamine content was increased consecutively. The as prepared composites were named as TC1 to TC6, while the mixing ratio of NP400 to melamine varied as 2:1, 1:1, 1:2, 1:3, 1:4, and 1:5 respectively. Similarly, another 4 samples were prepared by calcining the precursor mix at 600°C. The samples were termed as TC7, TC8 and TC9, while the mixing ratio of NP400 to melamine varied as 1:2, 1:3, and 1:4 respectively.

2.3 Characterization

The crystalline structure of the prepared composites was characterized by XRD analysis by generating XRD patterns on an MDI Jade 5.0 X-ray diffractometer (D/MAX Ultima III, Rigaku, Japan) with Cu Kα radiation source, operating at 40 kV and 40 mA. By using Bragg-Brentano experimental arrangement, the XRD pattern was recorded in the 2θ range of 2° to 90°, at a scanning rate of 0.02/sec. The limiting parameters of the X-ray beam were 2/3° divergence, 10 mm divergent height, 2/3◦ scattering, and 0.3 mm receiving slits.

The morphology of the powdered TiO_2/g-CN was studied by a SEM (S-4700, Hitachi, Japan), operating at 15 kV in vacuum at a working distance of 7 mm. The elemental compositions were estimated by using EDX detector (55VP SEM) operating at 15 kV. A field emission transmission electron microscope (FE-TEM, JEOL Ltd., JEM-2100F, Japan) operating at 200 kV was used to examine fine details of the samples' morphology. The TEM samples were prepared by evaporation in air of a droplet of the powders dispersed in ethanol onto Cu grid coated with holey carbon support films. N_2 adsorption-

desorption curves of the samples were developed using an automated surface area analyzer (Belsorp mini II, BEL, Japan), and the specific surface area was determined through Brunauer-Emmett-Teller (BET) method. The Barrett-Joyner-Halenda (BJH) model was also utilized for the calculation of mean pore diameter and the total pore volume by using the desorption isotherm at P/P_0=0.99. To perform the thermogravimetric analysis (TGA) and differential scanning calorimetry analysis (DSC), 5.04 mg of dry sample of the precursor mix (NP400:melamine = 1:1) was sealed in an aluminum crucible with a lid and scanned at a rate of 10°C/min. For DSC 1 heating and 1 cooling cycle was considered to observe the stability of the composite.

To identify g-CN and TiO_2 in the composite, the Fourier transform infrared (FT-IR) spectra (IRPrestige-21, Shimadzu, Japan) of the samples were taken in the wavenumber range of 400–4000 cm^{-1}. The KBr pellet preparation technique was utilized for the sample preparation. Also, to reveal the change in chemical bonds, X-ray photoelectron spectroscopy (XPS) data were collected in a Kratos Axis Ultra X-ray Photoelectron Spectroscopy system (MultiLab2000, VG, UK), using dry samples. To comment on the recombination rate of the photogenerated e^-/h^+ pairs in the as-prepared composites, photoluminescence (PL) spectra were generated in a microplate spectrofluorometer (Dual FL, Horiba, Piscataway, NJ, USA) by using the excitation wavelength of 300 nm. UV-Vis spectra were obtained using a UV-Vis-NIR spectrometer (Lambda 950, Perkin Elmer, KBSI Daegu center, South Korea) equipped with diffuse reflectance accessory. Spectra were recorded in the spectral range of 400–800 nm at a scan rate of 600 nm/min. The Kubelka-Munk function (F(R)) was employed to determine the optical bandgap of the prepared samples (see equations (1) – (3)). The direct and indirect energy bandgap was verified by extrapolation by plotting $(F(R)h\nu)^2$ vs hν and $(F(R)h\nu)^{1/2}$ vs hν, respectively.

$$F(R) = \frac{K}{S} \quad (1)$$

$$K = (1 - R)^2 \quad (2)$$

$$S = 2R \quad (3)$$

Here, K is the molar absorption coefficient, S is the scattering factor, and R is the reflectance data from DRS analysis.

2.4 Photocatalytic activity

A laboratory scale photocatalytic reactor was utilized to determine the NO_x (NO + NO_2) removal efficiency of the prepared composites under both UV and visible light irradiation. ISO 22197-1 (2007) and ISO 17198-1 (2018) were followed to conduct the photocatalytic NO_x removal analysis under UV and visible light respectively. All the composites were pre-treated under two 10 W UV-A (Sanyo-denki, Japan) lamps for 5 h with the light intensity of 10 W/m^2 ± 0.5 W/m^2. The details of the system are described elsewhere (Park et al., 2014; Rhee et al., 2018). A simple schematic of the experimental setup showing the utilized components and NO_x flow direction is provided in Fig. S1. Moreover, Fig. S1 illustrated the software interface of the NO_x analyzer that has been used for the study.

To place the powder samples in the photocatalytic reactor, a rectangular sample holder was used with a surface area of 50 cm^2, with 1 g of the prepared samples being pressed in the holder. By following ISO protocols, the experimental parameters of the reactor included a constant airflow of 3 L/min with 1 ppmv of NO at the inlet, moisture content of 50%, and internal temperature of 25 °C. At the outlet of the reactor a NO_x analyzer (CM2041, Casella) was fixed to determine the NO and NO_2 concentration. For photoactivity under visible light, a cool white fluorescent lamp with UV cut-off filter was utilized, with an illuminance of 6000 lx ± 300 lx. All the experiments were conducted for 100 min, where the light source was switched on after 20 min of gas adsorption and the light irradiance was continued for 1 h. The experiments were conducted in triplicates and the average values are reported in this study. The rate of NO removal, NO_x removal, NO_2 generation, and nitrate (NO_3^-) selectivity were determined using the following equations:

$$NO_{removal} = \frac{NO_{in} - NO_{out}}{NO_{in}} \quad (4)$$

$$NO_{2,generation} = \frac{NO_{2,out} - NO_{2,in}}{NO_{in}} \quad (5)$$

$$NO_{x,removal} = \frac{NO_{x,in} - NO_{x,out}}{NO_{in}} \quad (6)$$

$$NO_3^-{}_{selectivity} = \frac{NO_{x,removal}}{NO_{removal}} \times 100 \quad (7)$$

212 3 Result discussion

213 3.1 Morphological attributes

214 3.1.1 Phase structure and Transformation

215 The phase structure of each prepared composite tabulated in Table S1 was thoroughly investigated using
216 XRD. Fig. S1(a) and (b) illustrate the XRD patterns of the composites prepared by calcining at 550°C
217 and 600°C, respectively. For the composites prepared with varying temperature and precursor mix ratios,
218 the dominant diffraction peaks (2θ) represents the TiO_2 anatase crystal plans of (101), (103), (004),
219 (112), (200), (105), (211), (204), (116), (220), (215), and (224) respectively (JCPDS No. 21-1272)
220 (Giannakopoulou et al., 2017; Tan et al., 2018). The intensity of these peaks did not change significantly
221 with the increase of g-CN content. Also, the temperature variation from 550°C to 600°C does not show
222 any significant effect on the prevailing peaks of the anatase TiO_2 crystal peaks in the prepared
223 composites (Fig. S2). It should be noted that the diffraction peak positions of the used NP400 in the
224 precursor mix remained intact in the as-prepared composites, indicating no significant impacts on the
225 crystal phase from the incorporation of g-CN.

226 g-CN was prepared by polycondensation of melamine at both 550°C (g-CN1) and 600°C (g-CN2), to
227 compare the diffraction patterns with the prepared composites (Fig. S3). Three characteristic peaks
228 appear at 2θ ~ 13.04° (d = 0.693 nm), 17.82° and 27.58° (d = 0.324 nm) in g-CN1, representing the in-
229 plane repeating of tri-s-triazine units through trigonal N-bridging (100), meso g-CN crystal plane (600),
230 and the inter-planar staking of a conjugated aromatic system (002), respectively (Wang et al., 2015).
231 Notably, compared to g-CN1, the dominant (002) peak of g-CN2 shifted from 27.58° to 27.88° at higher
232 temperatures due to the decreased interlayer distance resulting from further polycondensation (Dong et
233 al., 2015).

(a) (b)

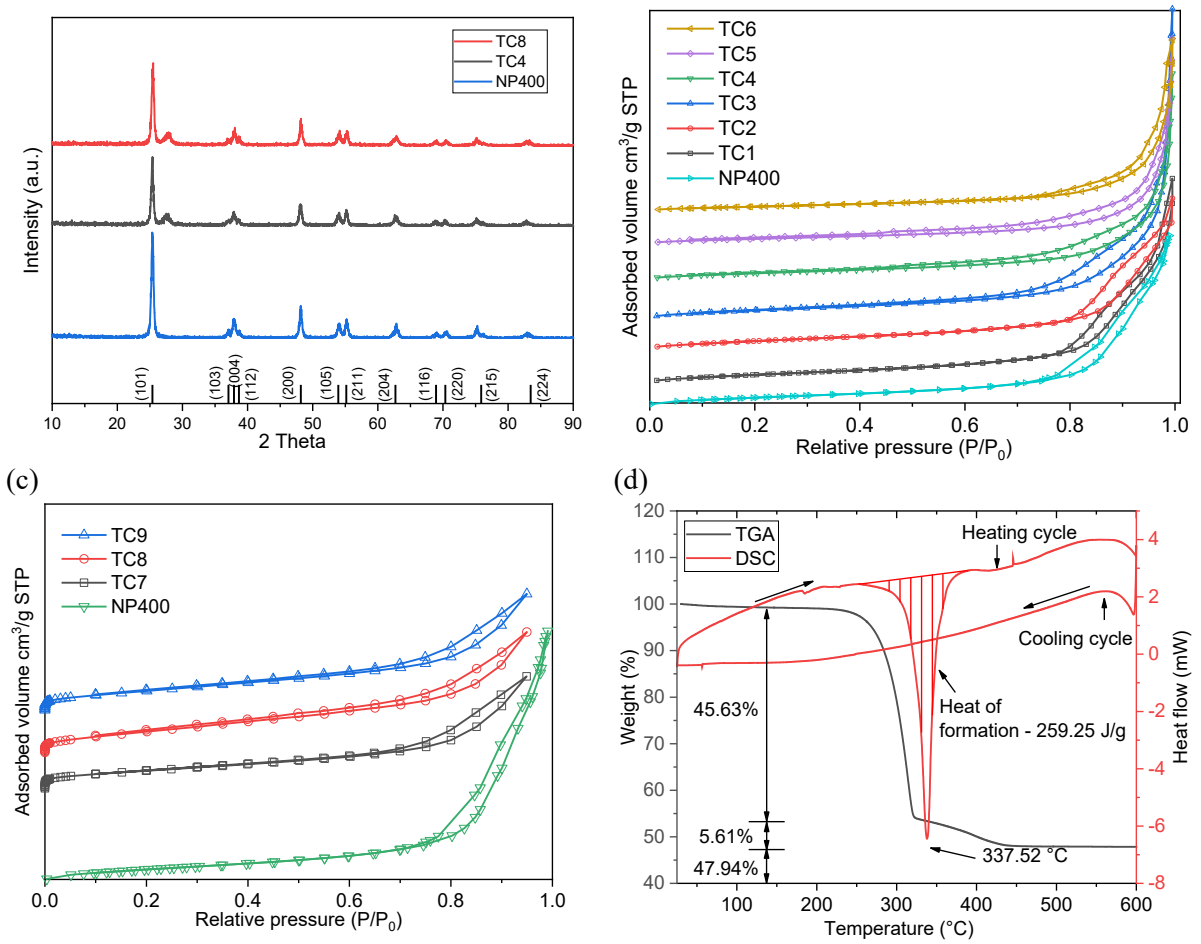

Fig. 1. (a) XRD patterns of NP400, TC4 and TC8; N_2 adsorption-desorption isotherms of the as-prepared composites (b) TC1 - TC6, and (c) TC7 - TC9 compared with NP400; (d) TGA and DSC data of the precursor mix of NP400:melamine = 1:1.

This evidence indicates that the g-CN stack is denser when melamine is heated to higher temperatures (Dong et al., 2011; Dong et al., 2015). Hence, the gallery distance between the graphene-like sheets of g-CN is reduced. Fig. S3 also indicates that the peak strength of diffraction is higher as the temperature of the pyrolysis increases. This rise in peak intensity means that, with higher polycondensation temperature, graphitic stacking of g-CN increases (Dong et al., 2015). Diffraction peaks for g-CN at 2θ ~ 27.58° corresponding to (002) the crystal phase of g-CN was observed in the composites when the melamine content in the precursor mix was twice that of NP400 (Fig. S2). Presumably, the low amounts of g-CN in TC1 and TC2 is the primary reason for this, where the mass loss of melamine by thermal decomposition is severe under air. Consequently, the increased dosage of melamine in the precursor confirmed the apparent presence of g-CN in the prepared composites, via broader and steeper (002)

peaks on the XRD pattern. Moreover, owing to a low concentration of g-CN in the as-prepared composites, the diffraction peaks around 13.04° and 17.82° seem to disappear in the diffraction pattern, which is congruent with relevant studies (Giannakopoulou et al., 2017; Kočí et al., 2017; Wei et al., 2017). The vanishing of the peak around 13.1° of prepared composites may have been caused primarily by the destruction of the in-plane periodic tri-s-triazine units (Dong et al., 2015).

Also, as a representative from sets of composites, Fig. 1 compared the XRD patterns of the composites TC4 and TC8 with NP400. TC4 and TC8 were prepared with the same precursor ratio (NP400: melamine = 1:3) but with different pyrolysis temperatures of 550°C and 600°C, respectively. From Fig. S2, it is clear that the composite catalysts prepared in this study were composed of the superposition of characteristic peaks of anatase TiO_2 and g-CN. This phenomenon inferred that g-CN was formed around NP400 through polymerization of the precursor melamine (Li et al., 2016; Wei et al., 2016). To further investigate the effects on crystal size of conjugated anatase TiO_2 due to the presence of g-CN, the crystal size of the as-prepared composites was calculated using Scherrer's equation (Zhou et al., 2019) and are tabulated in Table S2.

$$D = \frac{K\lambda}{FWHM \times \cos\theta} \quad (8)$$

Here, D is the crystallite size, λ is the wavelength of X-ray, K (0.9) is the crystal shape factor (Scherrer's constant) with a reference for a single crystal, θ is the Bragg angle, and FWHM is the full width at half maxima of the corresponding peak on the diffractogram. The crystal size was calculated for the dominant anatase TiO_2 peak around 25.28°. As shown in Table S2, no significant changes in the crystal size were observed with the increased proportion of g-CN in the composites. Additionally, the N_2 physisorption data of the as-prepared composites are presented in Fig. 1 (b) and (c). Moreover, the estimated productive surface areas (S_{BET}) and total pore volumes (V_T) are tabulated in Table S2. Referring to IUPAC classifications, the composites prepared by calcining at 550°C showed type IV isotherm with hysteresis loop of type H3 (Troppová et al., 2018). Nevertheless, the composites TC7 – TC9 (prepared @600°C) showed type IV isotherm with type H3 hysteresis loop. Both type H3 and H4 hysteresis loops confirm the presence of mesoporous structures in the as-prepared composites

(Thommes et al., 2015). Among the two sets of composites, prepared at varying temperatures, maximum S_{BET} was reported as 59.55 m^2/g and 43.64 m^2/g for TC3 and TC8, respectively.

TGA and DSC analysis was carried out to determine the phase transformation of the precursor mix of NP400 with melamine within the temperature range of 25°C to 600°C at a ramp of 10°C/min. During thermal analysis, an alumina crucible with a cover was used to replicate the real sample calcination thermal environment. Fig. 1(d) depicts the TGA and DSC data for the composite formation of TC2 as a representative, and clearly illustrates the phase transformations in the semi-closed system. The endothermic peak within the 323.01°C to 348.05°C range implies the thermal condensation of melamine into g-CN occurred within this range. The sharp initial decrease of 45.63% of the sample weight within the temperature range above can be attributed to melamine's condensation into melem (Thomas et al., 2008; Dong et al., 2014). The additional gradual reduction of weight by 5.61% around the peak of 337.52°C can be attributed to the condensation of melem to g-CN (Dong et al., 2014). To evaluate any phase transformation of the synthesized composite, one cooling cycle ran from 600°C to 25°C during DSC analysis, and no significant change was found. By integrating the area beneath the onset and end of the endothermic peak, the heat of formation for the prepared composite was assessed as 259.25 J/g.

3.1.2 FT-IR

FT-IR analysis was performed to verify the presence of TiO_2 and g-CN in the prepared composites. The FT-IR spectra of all the samples are shown in Fig. S4, where Fig. S4(a–b) and (c–d) present the FT-IR spectra for the composites prepared through pyrolysis at 550°C (TC1–TC6) and 600°C (TC7–TC9), respectively. Moreover, to compare the effects of different calcination temperatures, the FT-IR spectra of TC4, TC8, g-CN1, g-CN2, and NP400 are illustrated in Fig. 2. All the prepared composites (TC1–TC9), along with NP400, showed a broad peak around 400 – 700 cm^{-1}, which can be assigned to Ti-O-Ti bridge stretching and Ti-O stretching modes (Liu et al., 2019).

For the prepared g-CN1 and g-CN2, the characteristics adsorption band at 809.07 cm^{-1} and peak within the 1200 – 1670 cm^{-1} region was found (Fig. 2). The absorption band at 809.07 cm^{-1} can be attributed to out of plane skeletal bending modes of the triazine cycles (Zhang et al., 2018). Peaks at 1237.87, 1322.76, 1407.65, 1459.16, and 1568.72 cm^{-1} can be assigned to the aromatic C-N stretching, while the

peak at 1635.88 cm^{-1} can be ascribed to the C-N stretching mode (Troppová et al., 2018). The broad absorption band below 3000 – 3600 cm^{-1} was due to the N-H stretching vibration of the residual N-H (or NH_2) group bound to the sp^2 hybrid carbon or O-H stretching correlated with adsorbed H_2O (Du et al., 2019). Concerning the prepared composites except for TC1, all the characteristic adsorption peaks of g-CN were observed in the spectra (Fig. S4). Moreover, Fig. S4(a) and (c) showed that the relative intensity of the characteristic adsorption peaks for g-CN increased with higher melamine content in the precursor mix of the prepared composites. Furthermore, from the focused spectra (Fig. S4(b) and (c)), it can be found that the Ti-O-Ti stretching shifted slightly towards higher wavenumber along with the increase of g-CN content in the composites. That may be interpreted as the chemical environment of the anatase TiO_2 surface changing after combining with g-CN. It has been reported that when the connection between g-CN and TiO_2 becomes confined, the molecular orbitals of them may interact (Song et al., 2016). Consequently, the change in the chemical environment of anatase TiO_2 present in the composites may deduce strong heterojunction at the interface of TiO_2 and g-CN. These characterization results indicate the successful modification of TiO_2 by g-CN.

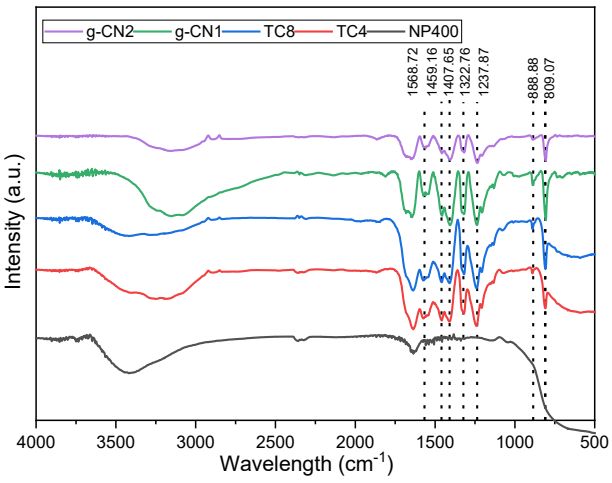

Fig. 2. FT-IR spectra of NP400, TC4, TC8 and g-CN2.

3.1.3 SEM and TEM

SEM and TEM were employed to identify the micromorphology and composition of the prepared composites. The SEM photos of the prepared composites are incorporated in Fig. S5 and S6. Fig. S5 (c – i) observed the existence of 2D layers like g-CN. It is clearly shown that g-CN consists of a 2D layer

organized morphology with a relatively smooth and flat surface. At the same time, for TiO_2 (Fig. S5(c – i)), a significant number of incompletely spaced spherical nanoparticles (NPs) are observed. Also, SEM was carried out on NP400, the precursor of anatase TiO_2 in the precursor mix, as illustrated in Fig. S6(a – c). By using the NP400 SEM, it can be observed that TiO_2 NPs are present as irregular spheres, and due to the influence of the nanometre, most particles agglomerate together (Yu et al., 2020). Consequently, the dispersity of TiO_2 nanoparticles formed on the surface of g-CN nanosheets increases compared with the pure NP400 nanoparticles (Fig. S6). The SEM and TEM of the prepared TC4 and TC8 are incorporated in Fig. 3. A TEM illustration of TC4 sample is shown in Fig. 3(c – d) to provide a better explanation of the nanostructure of the prepared composites. It can be seen in Fig 3 that TC4 has a lamellar structure, and the loaded TiO_2 NPs are distributed uniformly and densely without any apparent accumulation on the surface of g-CN nanosheets. That exhibits a strong hybrid effect between NP400 and g-CN. A significant number of TiO_2 NPs are homogeneously deposited on the surface of g-CN, which can be seen from Fig. 3(a) and (b). Also, the transparent lattice fringe of anatase TiO_2 nanoparticles with a d-spacing amidst 0.352 nm and 0.238 nm is found, which is due to the anatase TiO_2 lattice plane of (101) and (004) (Yu et al., 2020). The crystallization of TiO_2 and the intense interaction suggest that the heterojunction between TiO_2 and g-CN was successfully established.

(a)

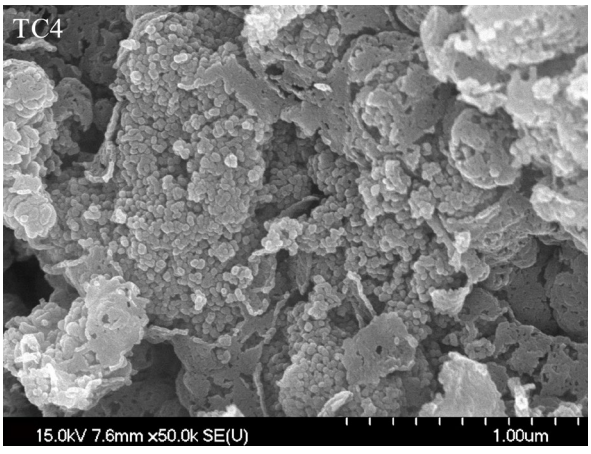

(b)

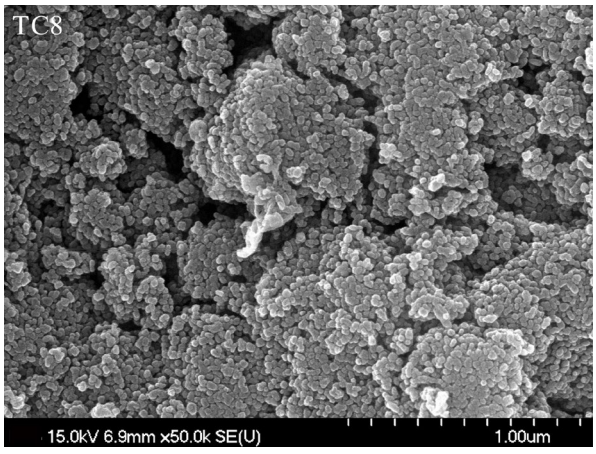

(c)

(d)

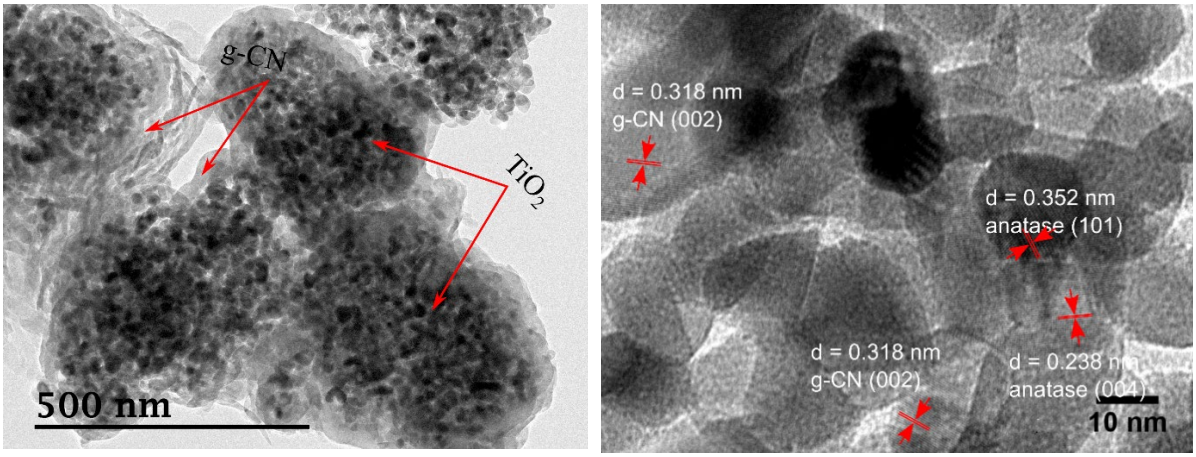

336 Fig. 3. SEM images of the as-prepared (a) TC4 and (b); (c-d) TEM of TC4 at varying magnification.

337 3.1.4 XPS

338 XPS analysis was conducted on the prepared samples to verify the surface chemical composition's
339 prevailing oxidation state. Fig. S7 presents the broad scan survey spectra of TC4, TC8, g-CN1, and g-
340 CN2. Based on the survey spectra, sharp photoelectron peaks are observed in TC4 and TC8 around the
341 binding energies of 287, 398, 458, and 529 eV, which can be attributed to C 1s, N 1s, Ti 2p, and O 1s
342 respectively (Zhou et al., 2014). Likewise, the g-CN1 and g-CN2 showed the corresponding C 1s and
343 N 1s spectra in the broad survey scan.

344 Fig. 4(a – d) illustrates the narrow scan spectra of the composites mentioned above. From the C 1s
345 spectra shown in Fig. 4(a), both g-CN1 and g-CN2 showed three deconvoluted peaks around 284.7,
346 286.4, and 288.08 eV. The deconvolution was conducted using Lorentz peak fitting. The peaks around
347 286.4 and 288.08 eV can be ascribed to C=N-C and N-C=N_2 coordination of g-CN (Zhou et al., 2014;
348 Kočí et al., 2017). Likewise, the C 1s spectra (Fig. 4(a)) of TC4 and TC8 showed the characteristic
349 peaks of g-CN around the binding energy of 284.7, 286.4 and 288.08 eV, and no significant peak shift
350 was observed.

351 From the high-resolution survey scan of N 1s (Fig. 4(b)), the as-prepared g-CN1 showed three
352 deconvoluted peaks around 398.54, 399.94 and 401.05 eV were observed, which can be ascribed to sp^2
353 hybridized C=N-C in the triazine rings, tertiary N-$(C)_3$, and N-H (i.e., hydrogen carrying amino function)
354 group respectively (Caudillo-Flores et al., 2019; Zhang et al., 2019b; Zhou et al., 2019). The prepared
355 g-CN2 showed similar peaks as g-CN1 along with the binding energies. However, due to a high degree

of polycondensation or close packing of π-electrons from the higher temperatures, the peak for the bridged nitrogen atom N-$(C)_3$ showed a negative shift of 0.7. The prepared composites TC4 and TC8 showed the presence of sp^2 hybridized C=N-C in the triazine rings, which confirms the successful development of g-CN in the composites. Compared to g-CN1 and g-CN2, the prepared composites TC4 and TC8 showed a positive peak shift of the narrowed N 1s scan towards higher binding energy, which could be attributed to the chemical environment change due to close interaction between NP400 and g-CN (Song et al., 2016). The observed peaks of O 1s spectra of NP400 fitted around the binding energies of 529.92 and 531.37 eV, which confirms the existence of TiO_2 and surface OH^- respectively (Huang et al., 2019; Li et al., 2019). Both the composites TC4 and TC8 confirm the presence of O2 by generating the narrow scan O 1s peak around 529.6 eV; however, a negative shift of 0.3 eV was observed, which is congruent with previous studies and confirms the successful formation of heterojunction between TiO_2 and g-CN (Song et al., 2016; Troppová et al., 2018).

Fig. 4(d) shows the Ti 2p spectra of commercially available NP400 in comparison with as-prepared composites TC4 and TC8. The prevailing peaks in NP400 around the binding energies of 458.66 and 464.41 eV ascribed to the Ti $2p_{3/2}$ and Ti $2p_{1/2}$, which confirms the original status of Ti is in the form of Ti^{4+} species (Giannakopoulou et al., 2017). Similar to O 1s spectra, a negative shift of 0.2 eV in Ti 2p peaks were observed for TC4. Due to the electronic interaction between NP400 and g-CN and varying electronegativity, an increased electron density on Ti could be the reason for this negative shift. The negative shift in binding energies was further increased in TC8 due to high calcination temperatures during synthesis in comparison to TC4.

(a) (b)

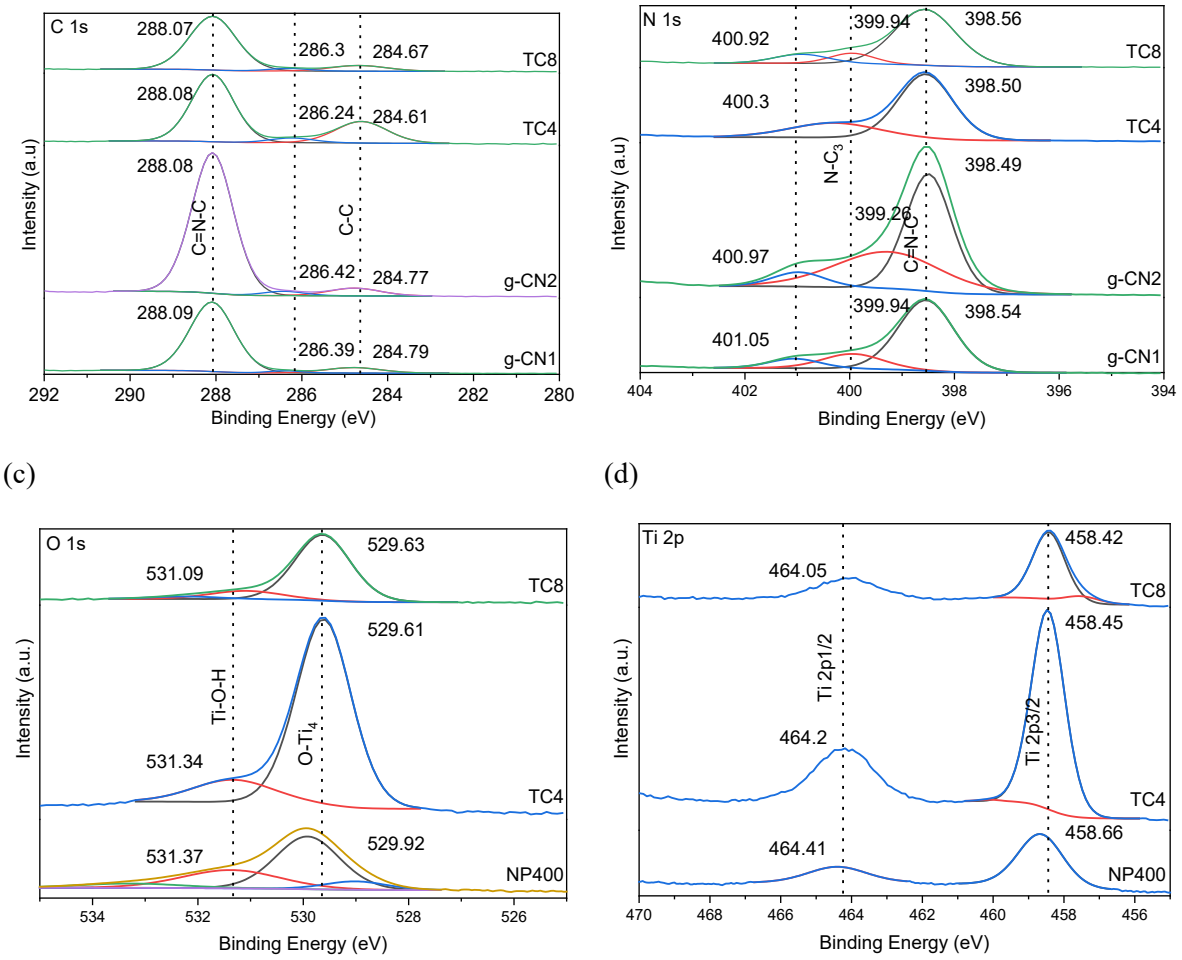

Fig. 4. High resolution survey scan of (a) C 1s, (b) N 1s, (c) O 1s, and (d) Ti 2p for TC4, TC8, g-CN1, g-CN2 and NP400.

3.2 Photocatalytic activities

Fig. S8(a) and S9(a) present the light assisted (UV/visible) NO_x removal patterns of TiO_2/g-CN composites prepared by calcining at 550°C. While, the Fig. S8(b) and S9(b) show results of the composites prepared by calcining at 600°C along with the NO_x removal profile of NP400, g-CN1, and g-CN2. As shown in Figures S6 and S7, the NO and NO_x concentrations started decreasing immediately after the initiation of irradiation (UV/visible). It is presumed that, from the beginning of the light radiation, NO is adsorbed and photocatalytically oxidized into NO_2 and NO_3^-. For the case of the conventional NP400, as shown in Fig. S8(b) (under UV irradiation) and Figure S9(b) (under visible light), the outflow of NO_x concentration reached a minimum within five minutes after light irradiation and later showed a gradual increase in the NO_x concentration. This result may be due to the majority of the surface area of the NP400 NPs starting to saturate with the photo-oxidation product (i.e., NO_3^-),

which would then increase the competition between the species on the limited photoreaction sites, thereby reducing the overall NO oxidation efficiency (Park et al., 2014; Rhee et al., 2018). The NO_x concentration instantly returned to the initial value when the light source was turned off after one-hour irradiation, indicating the transient physical adsorption of NO_x on the NP400 NPs. The total NO removal efficiencies for the NP400 during the one-hour irradiation of light was found to be 22.90% (Fig. 5(a)), and 9.37% (Fig. 5(b)) under UV and visible light, respectively.

Nonetheless, the as-prepared composites TC1 – TC9 showed a consistent NO removal profile under both UV and visible light irradiation, mainly due to varying nitrate selectivity compared to commercially available NP 400. Additionally, prepared g-CN1 and g-CN2 showed similar NO removal patterns as the composites, suggesting the dominance of g-CN in the composites concerning photoactivity. The graphs illustrated in Fig. 5(a – d) present the total percentage of NO removal, NO_x removal, NO_2 generation, and nitrate selectivity of the prepared composites under one-hour of UV and visible light irradiation, respectively.

For the composites prepared by calcining at 550℃ (TC1 – TC6), TC3 showed maximum NO removal of 36.67% under UV irradiation, which was approximately 1.60 and 3.44 times higher compared to NP400 and g-CN1. By considering the subsequent NO_2 production, the total NO_x removal using TC3 under UV irradiation was increased by 26.03% and 72.85% compared to NP400 and g-CN1, respectively. On the other hand, under visible light, although TC4 showed maximum NO removal of 34.05%, it was found inferior due to lower nitrate selectivity (48.31%). With nitrate selectivity of 57.6%, TC3 was found to remove 16.18% of NOx under visible light. That is approximately 74.39% and 78.92% higher than NP400 and g-CN1, respectively. Among the composites prepared by calcining at 600℃ (Fig. 5(c – d), TC8 showed maximum average NO and NO_x removal, both under UV and visible light. Under the UV light, TC8 showed a total NO_x removal of 14.74%, which was about 5.60% and 74.75% higher compared to NP400 and g-CN2, respectively. Successively, under visible light, the TC8 showed a significant increase of 66.00% compared to NP400, for NO_x removal.

The stability of TC3 as a representative composite was investigated by performing recycle experiments under UV light irradiation (Fig (e)). After five cycles, the photocatalytic activity showed negligible

decay, demonstrating the high stability and reusability of the as-prepared composites. However, the nitrate selectivity in consecutive runs showed a mild decreasing pattern confirming the presence of NO oxidized by-products on the active photocatalytic sites. After five cyclic run the nitrate selectivity reduced from 50.90% to 44.25%. To further investigate the mechanisms involved in photocatalysis UV-Vis DRS and PL analysis was conducted on TC3, TC4 and TC8.

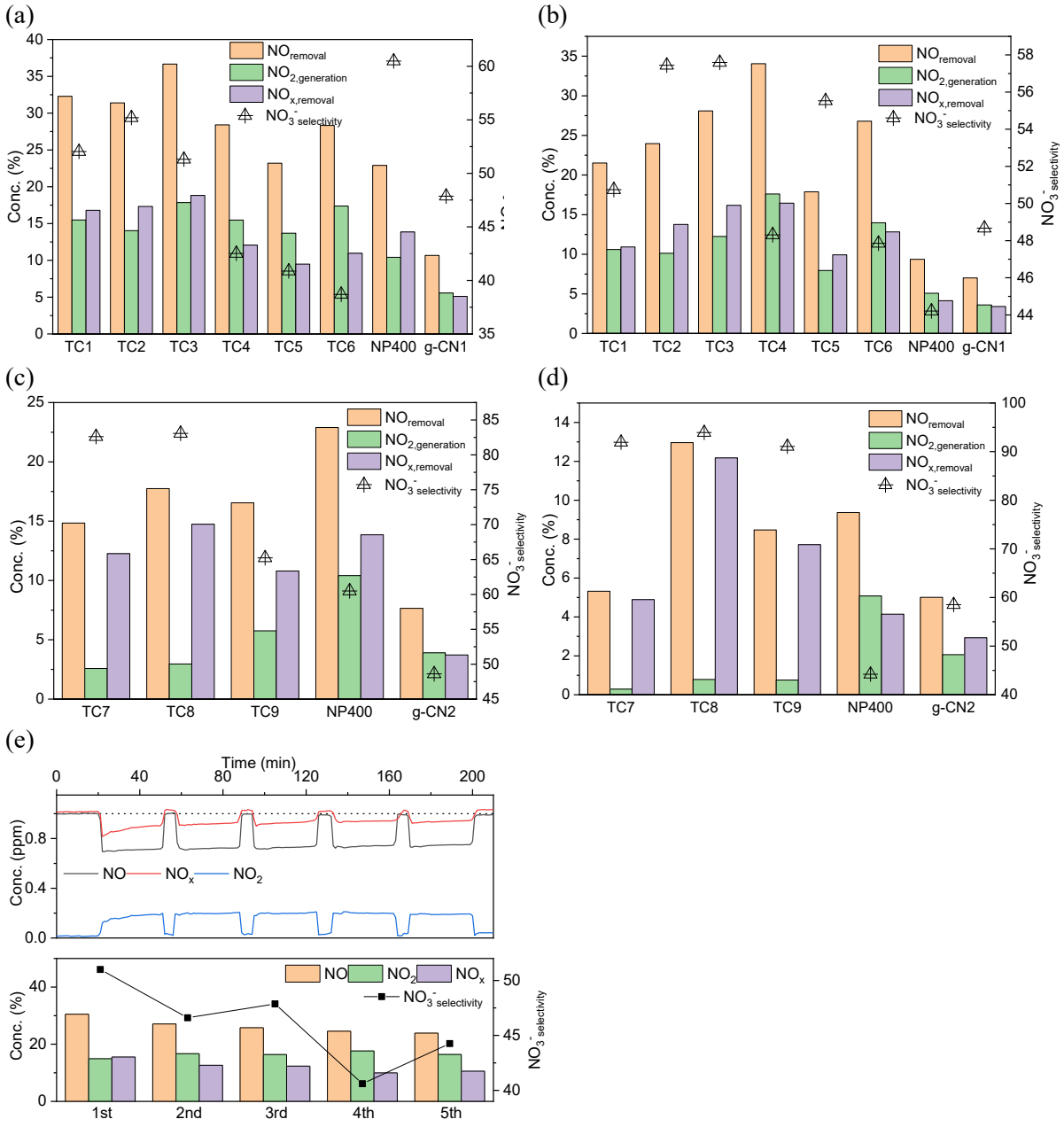

Fig. 5. Estimated $NO_{removal}$, $NO_{2,generation}$, $NO_{x,removal}$ and $NO_3^-{}_{selectivity}$ profile of (a – b) composites TC1 – TC6, NP400 and g-CN1, (c – d) composites TC7 – TC9, NP400 and g-CN2, under UV and visible light

irradiation, respectively; (e) Recycling experiments for NO removal under UV irradiation by using TC3 as a representative composite.

3.3 Optical properties

UV-Vis DRS was conducted to determine the energy bandgap of the prepared composites. Fig. 6(a) presents the absorbance spectra of NP400 and g-CN1, along with highly photoactive TC3, TC4, and TC8. The Kubelka-Munk function (F(R)) was employed to determine the energy bandgap (E_g) of the corresponding samples (see equation (1) – (3)) (Jiang et al., 2018). The energy bandgap was determined through extrapolation by plotting either $(F(R)h\nu)^2$ vs. hν or $(F(R)h\nu)^{1/2}$ vs. hν for direct and indirect bandgap respectively and has been illustrated in Fig. 6(b). Thus, the estimated bandgap values were 3.01, 2.81, 2.80, 2.66, and 2.72 eV for NP400, TC3, TC4, TC8, and g-CN1, respectively. In addition, the position of CB and VB of the semiconductors can be determined by using the following equations (Giannakopoulou et al., 2017; Huang et al., 2019):

$$E_{CB} = E_{VB} - E_g \quad (8)$$

$$E_{VB} = X - E_0 + 0.5\,E_g \quad (9)$$

Where E_{CB} and E_{VB} are CB and VB potential, X is the mean (geometric mean of the component atoms) electronegativity of the semiconductor, E_0 is the energy of free electrons against normal hydrogen electrode (NHE), and E_g is the energy bandgap of the semiconductor. From literature, the value of X can be ascribed as 5.81 and 4.64 eV for TiO_2 and g-CN, respectively, while E_0 is 4.5 eV (Kočí et al., 2017). For this study the CB and VB of NP400 was estimated as -0.20 and +2.81 eV (NHE, pH 7), respectively, while that of g-CN was about -1.22 and +1.50 eV, respectively. From Fig. 6(a), it is obvious that the heterojunction between NP400 and g-CN significantly enhanced the absorption edge of the composites in both UV and visible regions, similar traits were observed in the composites prepared heterojunction of P25 and melamine/urea (Wang et al., 2015; Ma et al., 2016; Sun et al., 2019). The maximum enhancement (both UV and visible region) has been observed in TC8; hence it showed increased photoactivity under light irradiation, irrespective of the wavelength region of the irradiated

light (see Fig. 5(c) and (d)). While TC3 and TC4 depicted equally narrowed energy bandgap, but, TC3 showed superior nitrate selectivity compared to TC4.

Consequently, for all the prepared composites along with NP400, g-CN1 and g-CN2, PL analysis was conducted at a fixed excitation wavelength (300 nm), and the results are illustrated in Fig. 6(c) and (d). As the PL spectra of a semiconductor give away the rate of recombination of the photogenerated e^-/h^+ pairs, it can assist in describing the level of photoactivity (Wang et al., 2013; Yu et al., 2013b). The composites synthesized by calcining at 550°C and 600°C showed a large semi-asymmetric band around the maximum wavelength of 438.74 nm and 443.20 nm, respectively. The redshift in the PL spectra supports the extended light absorption by TC8 in the visible range and narrower energy bandgap illustrated in Fig. 6(a) and (b) respectively. Moreover, the redshift suggested the high degree of condensation of the g-CN incorporated in the composites (Thomas et al., 2008). The reported PL spectra can be explained as the transition of e^- in between the antibonding pi states and lone pair states of the prevailing atoms (Dai et al., 2013; Stroyuk et al., 2015; Zhang et al., 2015). By using Fig. 6(c) and (d), the order of PL intensities of the tested semiconductors can be shown as g-CN1>TC5>TC4>TC3 and g-CN3>TC7>TC8>TC9. Due to the successful formation of heterojunction between NP400 and g-CN, PL intensity reduced in the prepared composites compared to g-CN1 and g-CN2.

(a)

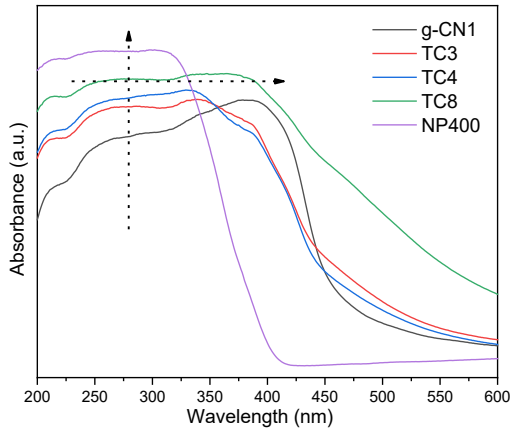

(b)

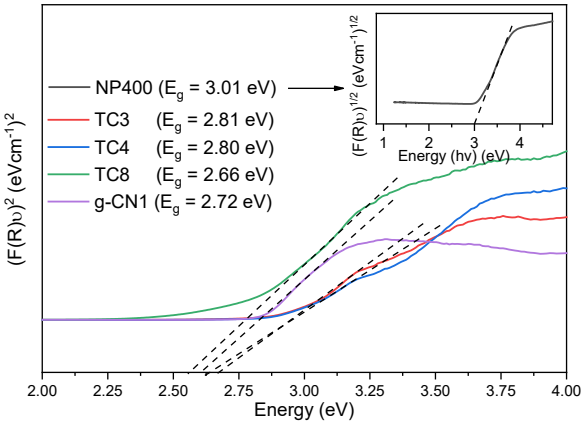

(c)

(d)

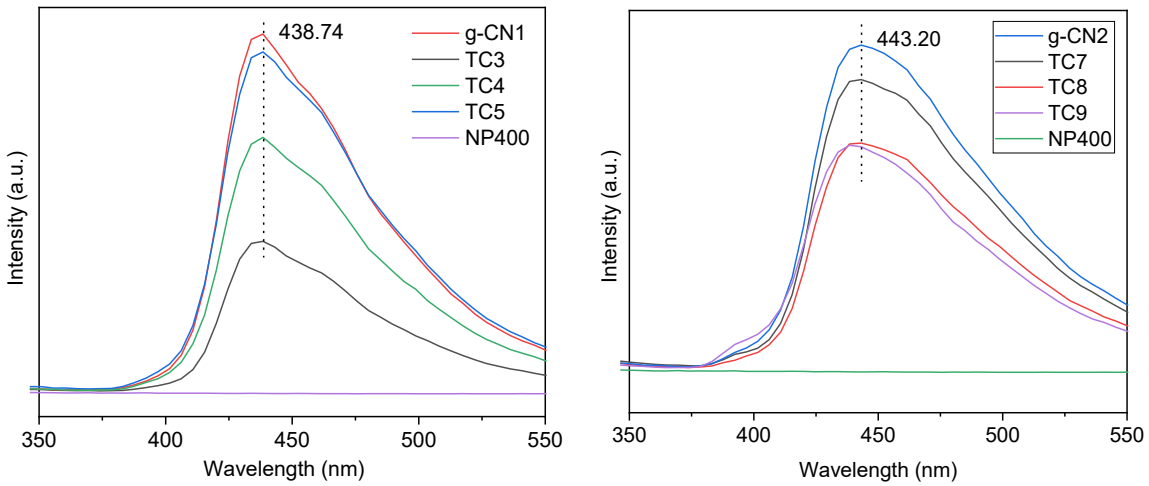

Fig. 6. (a) UV-Vis DRS spectra, (b) converted Kubelka-Munk function vs. energy of absorbed light; PL spectra of the as prepared composites (c) TC3 – TC5, and (d) TC7 – TC9 compared with NP400, g-CN1 and g-CN2.

3.4 NO removal mechanism

Based on the structural and optical characterizations, it can be deduced that the superior photocatalytic activities of the as-prepared composites are attributed to available photocatalytic sites due to the preferable surface area, tailored energy bandgaps, and inhibited e^-/h^+ pair recombination rates. The specific surface area of the as-prepared composites showed a sinusoidal pattern initially increased with the incorporation of g-CN in the composites and started to decrease when the melamine content in the precursor mix was four times than that of NP400. For the composites prepared at 550°C (TC1 – TC6), the dominance of surface area was observed during photocatalytic NO removal. Maximum NO removal of 36.66% was reached when the S_{BET} value was 59.55 m^2/g, and later started to decrease with the decline in S_{BTE}. Interestingly, despite having similar S_{BET} values (see Table S2), the composites prepared by calcining at 600°C showed sinusoidal influence for photo-oxidation of NO under UV/visible light. This phenomenon portrays the dominance of optical attributes compared to structural ones for the composites TC7 to TC9.

Compared to NP400, g-CN1, and g-CN2, all the prepared composites showed superior NO oxidation under both UV, and visible irradiation, which is evident as the light absorption attribute of the composites was enhanced throughout the UV-Vis region of the light spectrum (Fig. 6(a)). By

considering the varying synthesis temperature, the maximum NO_x removal was observed in TC3 (synthesized @ 550°C), and TC8 (synthesized @ 600°C), in which the corresponding NP400 to melamine ratio was 1:2 and 1:3 respectively. Intriguingly, TC4 showed maximum NO oxidation under visible light, but the lower nitrate selectivity made TC3 the best option among TC1–TC6.

It is widely agreed that photocatalytic NO oxidation comprises mostly the active species such as superoxide ($\cdot O_2^-$) and hydroxyl ($\cdot OH$) radicals, which are generated from the redox reactions involving the photogenerated e^-/h^+ pairs and adsorbed O_2 and OH^- groups in the NPs (Troppová et al., 2018). Based on the literature, the pathway of NO oxidation over a photocatalyst can be expressed as follows (Song et al., 2016; Papailias et al., 2017; Troppová et al., 2018):

$$Photocatalyst + h\vartheta \rightarrow e^- + h^+ \quad (10)$$

$$e^- + O_2 \rightarrow \cdot O_2^- \quad (11)$$

$$h^+ + OH^- \rightarrow \cdot OH \quad (12)$$

$$\cdot O_2^- + NO \rightarrow NO_3^- \quad (13)$$

$$\cdot OH + NO \rightarrow NO_2 \quad (14)$$

$$\cdot OH + NO_2 \rightarrow NO_3^- \quad (15)$$

For the photogenerated e^- to produce $\cdot O_2^-$ effectively, the CB edge of the photocatalyst must be more negative compared to the redox potential of $O_2/\cdot O_2^-$ (0.33 eV vs. NHE) (Du et al., 2019). Alternatively, the standard redox potential for $OH^-/\cdot OH$ is 1.99 eV against NHE; hence, the position of VB needed to be more positive for the h^+ to generate $\cdot OH$ radicals (Giannakopoulou et al., 2017; Kočí et al., 2017).

For this study the CB and VB of NP400 was estimated as -0.20 and +2.81 eV (NHE, pH 7), respectively, while that of g-CN was about −1.22 and +1.50 eV, respectively. Based on the estimated CB and VB positions of NP400 and g-CN, a simple schematic of NO oxidation was proposed for the prepared composite and illustrated in Fig. 7. Under UV light irradiation, both NP400 and g-CN present in the composite could get excited and could generate photogenerated e^-/h^+ pairs, as shown in Fig. 7. Due to the bandgap disparity, the h^+ generated on the VB of NP400 can transfer to the VB of g-CN, while the

e^- generated on CB of g-CN and move to the CB of NP400 (Ma et al., 2016; Papailias et al., 2017). Hence the recombination rate of the UV generated e^-/h^+ pairs get inhibited. The photogenerated e^- can readily produce $\cdot O_2^-$ by reacting with adsorbed O_2 and the h^+ on the VB can directly oxidize H_2O/OH^- to $\cdot OH$ radicals. It has been inferred that the $\cdot O_2^-$ and $\cdot OH$ radicals are the primary component to successfully oxidize NO to neutral component NO_3^- (Song et al., 2016). On the other hand, when the prepared composite was exposed to visible light, only g-CN got excited, and the photogenerated e^- on the CB could transfer to VB of NP400 due to the bandgap offset. However, the h^+ generated on the VB of g-CN could remain on the VB and can migrate to the surface of the composite to directly oxidize NO_x (Song et al., 2016).

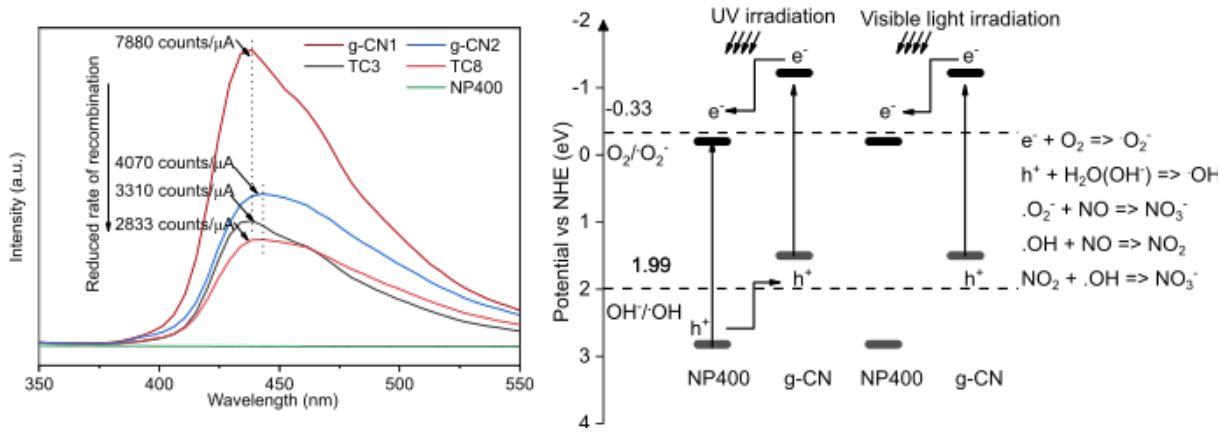

Fig. 7. Proposed schematic of NO removal mechanism for the prepared TiO_2/g-CN composites

4 Conclusion

The objective of the study was to prepare an enhanced photoactive TiO_2/g-CN composite within both a UV and visible light spectrum for the efficient degradation of atmospheric NO_x. TiO_2/g-CN composites were successfully prepared through a simple calcination route by using NP400 and melamine as the precursors. It has been noted that the incorporation of g-CN with NP400 greatly enhanced the optical traits of the composites. By using the UV-visible DRS technique, we have confirmed that the absorption bands of the prepared composites were significantly enhanced in both UV and visible light regions compared to NP400 and g-CN, respectively. The energy bandgap of the prepared composites narrowed

and was determined to be at a favourable position to generate $^{\cdot}O_2^-$ and $^{\cdot}OH$ radicals readily for photodegradation of NO_x. TC3 and TC8 were found as the optimal composites based on NO_x oxidation potentials, and the corresponding energy bandgaps were found as 2.88 eV and 2.66 eV, respectively. One of the interesting findings was, higher calcination temperature for the synthesis of the composites affected the nitrate selectivity positively (less NO_2 generation). A significant reduction in NO_2 production was observed irrespective of the light irradiation. For instance, for TC7, TC8, and TC9 (i.e., composites prepared by calcining at 600°C) the NO_2 generation rates after one-hour of UV light irradiation were only 2.58%, 2.96%, and 5.75% respectively, which were 0.29%, 0.78%, and 0.75% under visible light irradiation. Hence, enhancement in calcination temperature during the preparation of TiO_2/g-CN composites could play a decisive role in minimizing the NO_2 release during photo-oxidation of NO_x, irrespective of the light source of photocatalysis.

Author contribution statement

Conceptualization and methodology, S.M.H., H.P. and J.S.M.; data analysis, investigation and data curation, S.M.H., J.S.M. and I.R.; original draft writing, S.M.H.; review and editing, L.T., H.-J.K., Y.-S.J. and H.K.S.; supervision, J.-H.K., H.K.S and Y.-S.J. All authors provided critical feedback and helped shape the research, analysis and manuscript.

Declaration of competing interest

The authors declare that they have no known competing financial interests or personal relationships that could have appeared to influence the work reported in this paper.

Acknowledgements

This research was supported by a grant (18SCIP-B145909-01) from Smart Civil Infrastructure Research Program funded by Ministry of Land, Infrastructure and Transport of Korean government.

References

Caudillo-Flores, U., Muñoz-Batista, M.J., Luque, R., Fernández-García, M., Kubacka, A., 2019. g-C3N4/TiO2 composite catalysts for the photo-oxidation of toluene: Chemical and charge handling effects. Chemical Engineering Journal 378.

554 Cui, L., Liu, S., Wang, F., Li, J., Song, Y., Sheng, Y., Zou, H., 2020. Growth of uniform g-C3N4 shells
555 on 1D TiO2 nanofibers via vapor deposition approach with enhanced visible light photocatalytic
556 activity. Journal of Alloys and Compounds 826.
557 Dai, H., Gao, X., Liu, E., Yang, Y., Hou, W., Kang, L., Fan, J., Hu, X., 2013. Synthesis and
558 characterization of graphitic carbon nitride sub-microspheres using microwave method under mild
559 condition. Diamond Relat. Mater. 38, 109-117.
560 Damma, D., Boningari, T., Ettireddy, P.R., Reddy, B.M., Smirniotis, P.G., 2018. Direct Decomposition
561 of NOX over TiO2 Supported Transition Metal Oxides at Low Temperatures. Industrial & Engineering
562 Chemistry Research 57, 16615-16621.
563 deKrafft, K.E., Wang, C., Lin, W., 2012. Metal-organic framework templated synthesis of Fe2O3/TiO2
564 nanocomposite for hydrogen production. Adv Mater 24, 2014-2018.
565 Dong, F., Li, Y., Wang, Z., Ho, W.-K., 2015. Enhanced visible light photocatalytic activity and
566 oxidation ability of porous graphene-like g-C3N4 nanosheets via thermal exfoliation. Applied Surface
567 Science 358, 393-403.
568 Dong, F., Ou, M.Y., Jiang, Y.K., Guo, S., Wu, Z.B., 2014. Efficient and Durable Visible Light
569 Photocatalytic Performance of Porous Carbon Nitride Nanosheets for Air Purification. Industrial &
570 Engineering Chemistry Research 53, 2318-2330.
571 Dong, F., Wang, Z.Y., Sun, Y.J., Ho, W.K., Zhang, H.D., 2013. Engineering the nanoarchitecture and
572 texture of polymeric carbon nitride semiconductor for enhanced visible light photocatalytic activity.
573 Journal of Colloid and Interface Science 401, 70-79.
574 Dong, F., Wu, L., Sun, Y., Fu, M., Wu, Z., Lee, S.C., 2011. Efficient synthesis of polymeric g-C3N4
575 layered materials as novel efficient visible light driven photocatalysts. Journal of Materials Chemistry
576 21.
577 Du, X., Bai, X., Xu, L., Yang, L., Jin, P., 2019. Visible-light activation of persulfate by TiO2/g-C3N4
578 photocatalyst toward efficient degradation of micropollutants. Chemical Engineering Journal.
579 Giannakopoulou, T., Papailias, I., Todorova, N., Boukos, N., Liu, Y., Yu, J., Trapalis, C., 2017.
580 Tailoring the energy band gap and edges' potentials of g-C_3N_4/TiO_2 composite photocatalysts for NO_x
581 removal. Chemical Engineering Journal 310, 571-580.

582 Huang, J., Li, D., Li, R., Chen, P., Zhang, Q., Liu, H., Lv, W., Liu, G., Feng, Y., 2020. One-step
583 synthesis of phosphorus/oxygen co-doped g-C3N4/anatase TiO2 Z-scheme photocatalyst for
584 significantly enhanced visible-light photocatalysis degradation of enrofloxacin. J Hazard Mater 386,
585 121634.
586 Huang, Q., Hu, Y., He, G., Lin, C., Wei, C., 2018. Photocatalytic oxidation of nitrogen oxides over
587 {001}TiO2: the influence of F- ions. Environmental Science and Pollution Research 25, 35342-35351.
588 Huang, Y., Wang, P.G., Wang, Z.Y., Rao, Y.F., Cao, J.J., Pu, S.Y., Ho, W.K., Lee, S.C., 2019.
589 Protonated g-C3N4/Ti( )(3+)self-doped TiO2 nanocomposite films: Room-temperature preparation,
590 hydrophilicity, and application for photocatalytic NOx removal. Appl. Catal. B-Environ. 240, 122-131.
591 Jiang, G.M., Cao, J.W., Chen, M., Zhang, X.M., Dong, F., 2018. Photocatalytic NO oxidation on N-
592 doped TiO2/g-C3N4 heterojunction: Enhanced efficiency, mechanism and reaction pathway. Applied
593 Surface Science 458, 77-85.
594 Kočí, K., Reli, M., Troppová, I., Šihor, M., Kupková, J., Kustrowski, P., Praus, P., 2017. Photocatalytic
595 decomposition of N2O over TiO2/g-C3N4 photocatalysts heterojunction. Applied Surface Science 396,
596 1685-1695.
597 Li, C., Lou, Z., Yang, Y., Wang, Y., Lu, Y., Ye, Z., Zhu, L., 2019. Hollowsphere Nanoheterojunction
598 of g-C3N4@TiO2 with High Visible Light Photocatalytic Property. Langmuir 35, 779-786.
599 Li, C., Sun, Z., Xue, Y., Yao, G., Zheng, S., 2016. A facile synthesis of g-C3N4/TiO2 hybrid
600 photocatalysts by sol–gel method and its enhanced photodegradation towards methylene blue under
601 visible light. Advanced Powder Technology 27, 330-337.
602 Li, Y.H., Sun, Y.J., Ho, W.K., Zhang, Y.X., Huang, H.W., Cai, Q., Dong, F., 2018. Highly enhanced
603 visible-light photocatalytic NOx purification and conversion pathway on self-structurally modified g-
604 C3N4 nanosheets. Science Bulletin 63, 609-620.
605 Liu, H., Yu, D.Q., Sun, T.B., Du, H.Y., Jiang, W.T., Muhammad, Y., Huang, L., 2019. Fabrication of
606 surface alkalinized g-C3N4 and TiO2 composite for the synergistic adsorption-photocatalytic
607 degradation of methylene blue. Applied Surface Science 473, 855-863.
608 Lu, X., Wang, Q., Cui, D., 2010. Preparation and Photocatalytic Properties of g-C3N4/TiO2 Hybrid
609 Composite. Journal of Materials Science & Technology 26, 925-930.

Ma, J.Z., Wang, C.X., He, H., 2016. Enhanced photocatalytic oxidation of NO over g-C3N4-TiO2 under UV and visible light. Appl. Catal. B-Environ. 184, 28-34.

Mamaghani, A.H., Haghighat, F., Lee, C.S., 2017. Photocatalytic oxidation technology for indoor environment air purification: The state-of-the-art. Appl. Catal. B-Environ. 203, 247-269.

Martinez-Oviedo, A., Ray, S.K., Hoang Phuc, N., Lee, S.W., 2019. Efficient photo-oxidation of NO_x by Sn doped blue TiO_2 nanoparticles. Journal of Photochemistry and Photobiology a-Chemistry 370, 18-25.

Oskooei, A.B., Koohsorkhi, J., Mehrpooya, M., 2019. Simulation of plasma-assisted catalytic reduction of NOx, CO, and HC from diesel engine exhaust with COMSOL. Chem. Eng. Sci. 197, 135-149.

Pan, J.H., Zhao, X.S., Lee, W.I., 2011. Block copolymer-templated synthesis of highly organized mesoporous TiO2-based films and their photoelectrochemical applications. Chemical Engineering Journal 170, 363-380.

Papailias, I., Todorova, N., Giannakopoulou, T., Yu, J.G., Dimotikali, D., Trapalis, C., 2017. Photocatalytic activity of modified g-C3N4/TiO2 nanocomposites for NOx removal. Catalysis Today 280, 37-44.

Park, S.M., Chekli, L., Kim, J.B., Shahid, M., Shon, H.K., Kim, P.S., Lee, W.S., Lee, W.E., Kim, J.H., 2014. NO_x removal of mortar mixed with titania produced from Ti-salt flocculated sludge. Journal of Industrial and Engineering Chemistry 20, 3851-3856.

Rhee, I., Lee, J.S., Kim, J.B., Kim, J.H., 2018. Nitrogen oxides mitigation efficiency of cementitious materials incorporated with TiO 2. Materials 11.

Schwartz-Narbonne, H., Jones, S.H., Donaldson, D.J., 2019. Indoor lighting releases gas phase nitrogen oxides from indoor painted surfaces. Environmental Science & Technology Letters 6, 92-97.

Song, W., Zeng, Y., Wang, Y., Zhang, S., Zhong, Q., Wang, T., Wang, X., 2019. Photo-induced strong active component-support interaction enhancing NO_x removal performance of CeO_2/TiO_2. Applied Surface Science 476, 834-839.

Song, X., Hu, Y., Zheng, M.M., Wei, C.H., 2016. Solvent-free in situ synthesis of g-C3N4/{001}TiO2 composite with enhanced UV- and visible-light photocatalytic activity for NO oxidation. Appl. Catal. B-Environ. 182, 587-597.

638 Stroyuk, A.L., Panasiuk, Y.V., Raevskaya, A.E., Kuchmy, S.Y., 2015. Spectral and Luminescent
639 Characteristics of Products from Exfoliation of Graphitic Carbon Nitride Produced at Various
640 Temperatures. Theor. Exp. Chem. 51, 243-251.
641 Sun, Q., Hu, X., Zheng, S., Zhang, J., Sheng, J., 2019. Effect of calcination on structure and
642 photocatalytic property of N-TiO2/g-C3N4@diatomite hybrid photocatalyst for improving reduction of
643 Cr(). Environ Pollut 245, 53-62.
644 Tan, S., Xing, Z., Zhang, J., Li, Z., Wu, X., Cui, J., Kuang, J., Zhu, Q., Zhou, W., 2018. Ti3+-TiO2/g-
645 C3N4 mesostructured nanosheets heterojunctions as efficient visible-light-driven photocatalysts.
646 Journal of Catalysis 357, 90-99.
647 Thomas, A., Fischer, A., Goettmann, F., Antonietti, M., Müller, J.-O., Schlögl, R., Carlsson, J.M., 2008.
648 Graphitic carbon nitride materials: variation of structure and morphology and their use as metal-free
649 catalysts. Journal of Materials Chemistry 18.
650 Thommes, M., Kaneko, K., Neimark, A.V., Olivier, J.P., Rodriguez-Reinoso, F., Rouquerol, J., Sing,
651 K.S.W., 2015. Physisorption of gases, with special reference to the evaluation of surface area and pore
652 size distribution (IUPAC Technical Report). Pure and Applied Chemistry 87, 1051-1069.
653 Troppová, I., Šihor, M., Reli, M., Ritz, M., Praus, P., Kočí, K., 2018. Unconventionally prepared TiO
654 2 /g-C 3 N 4 photocatalysts for photocatalytic decomposition of nitrous oxide. Applied Surface Science
655 430, 335-347.
656 Tsang, C.H.A., Li, K., Zeng, Y., Zhao, W., Zhang, T., Zhan, Y., Xie, R., Leung, D.Y.C., Huang, H.,
657 2019. Titanium oxide based photocatalytic materials development and their role of in the air pollutants
658 degradation: Overview and forecast. Environment International 125, 200-228.
659 Wang, H., Li, J., Ma, C., Guan, Q., Lu, Z., Huo, P., Yan, Y., 2015. Melamine modified P25 with heating
660 method and enhanced the photocatalytic activity on degradation of ciprofloxacin. Applied Surface
661 Science 329, 17-22.
662 Wang, X.-j., Yang, W.-y., Li, F.-t., Xue, Y.-b., Liu, R.-h., Hao, Y.-j., 2013. In Situ Microwave-Assisted
663 Synthesis of Porous N-TiO2/g-C3N4 Heterojunctions with Enhanced Visible-Light Photocatalytic
664 Properties. Industrial & Engineering Chemistry Research 52, 17140-17150.

Wang, Z.Y., Chen, M.J., Huang, Y., Shi, X.J., Zhang, Y.F., Huang, T.T., Cao, J.J., Ho, W.K., Lee, S.C., 2018. Self-assembly synthesis of boron-doped graphitic carbon nitride hollow tubes for enhanced photocatalytic NOx removal under visible light. Appl. Catal. B-Environ. 239, 352-361.

Wei, X., Shao, C., Li, X., Lu, N., Wang, K., Zhang, Z., Liu, Y., 2016. Facile in situ synthesis of plasmonic nanoparticles-decorated g-C3N4/TiO2 heterojunction nanofibers and comparison study of their photosynergistic effects for efficient photocatalytic H2 evolution. Nanoscale 8, 11034-11043.

Wei, Z., Liang, F., Liu, Y., Luo, W., Wang, J., Yao, W., Zhu, Y., 2017. Photoelectrocatalytic degradation of phenol-containing wastewater by TiO2/g-C3N4 hybrid heterostructure thin film. Applied Catalysis B: Environmental 201, 600-606.

Xia, Y., Xu, L., Peng, J., Han, J., Guo, S., Zhang, L., Han, Z., Komarneni, S., 2019. TiO2@g-C3N4 core/shell spheres with uniform mesoporous structures for high performance visible-light photocatalytic application. Ceramics International 45, 18844-18851.

Yan, H., Yang, H., 2011. TiO2–g-C3N4 composite materials for photocatalytic H2 evolution under visible light irradiation. Journal of Alloys and Compounds 509, L26-L29.

Yang, L., Hakki, A., Zheng, L., Jones, M.R., Wang, F., Macphee, D.E., 2019. Photocatalytic concrete for NO_x abatement: Supported TiO_2 efficiencies and impacts. Cement and Concrete Research 116, 57-64.

Yu, B., Meng, F., Khan, M.W., Qin, R., Liu, X., 2020. Facile synthesis of AgNPs modified TiO2@g-C3N4 heterojunction composites with enhanced photocatalytic activity under simulated sunlight. Materials Research Bulletin 121.

Yu, H., Pan, J., Bai, Y., Zong, X., Li, X., Wang, L., 2013a. Hydrothermal synthesis of a crystalline rutile TiO2 nanorod based network for efficient dye-sensitized solar cells. Chemistry 19, 13569-13574.

Yu, J., Wang, S., Low, J., Xiao, W., 2013b. Enhanced photocatalytic performance of direct Z-scheme g-C3N4-TiO2 photocatalysts for the decomposition of formaldehyde in air. Phys Chem Chem Phys 15, 16883-16890.

Zhang, B., Wang, Q., Zhuang, J., Guan, S., Li, B., 2018. Molten salt assisted in-situ synthesis of TiO2/g-C3N4 composites with enhanced visible-light-driven photocatalytic activity and adsorption ability. Journal of Photochemistry and Photobiology A: Chemistry 362, 1-13.

693 Zhang, S., Gu, P.C., Ma, R., Luo, C.T., Wen, T., Zhao, G.X., Cheng, W.C., Wang, X.K., 2019a. Recent
694 developments in fabrication and structure regulation of visible-light-driven g-C3N4-based
695 photocatalysts towards water purification: A critical review. Catalysis Today 335, 65-77.
696 Zhang, X.B., Song, H.Y., Sun, C.Y., Chen, C.X., Han, F.Q., Li, X.F., 2019b. Photocatalytic oxidative
697 desulfurization and denitrogenation of fuels over sodium doped graphitic carbon nitride nanosheets
698 under visible light irradiation. Materials Chemistry and Physics 226, 34-43.
699 Zhang, Z., Wu, S., Zhang, J., Tang, S., Hu, C., Li, Y., Jiang, L., Cui, Q., 2015. Well-aligned carbon
700 nitride nanorods: the template-free synthesis and their optical and thermal properties. Appl. Phys. A
701 119, 1507-1513.
702 Zhang, Z.Q., Bai, L.L., Li, Z.J., Qu, Y., Jing, L.Q., 2019c. Review of strategies for the fabrication of
703 heterojunctional nanocomposites as efficient visible-light catalysts by modulating excited electrons
704 with appropriate thermodynamic energy. Journal of Materials Chemistry A 7, 10879-10897.
705 Zhou, B., Hong, H., Zhang, H., Yu, S., Tian, H., 2019. Heterostructured Ag/g-C3N4/TiO2 with
706 enhanced visible light photocatalytic performances. Journal of Chemical Technology & Biotechnology
707 94, 3806-3814.
708 Zhou, S., Liu, Y., Li, J., Wang, Y., Jiang, G., Zhao, Z., Wang, D., Duan, A., Liu, J., Wei, Y., 2014.
709 Facile in situ synthesis of graphitic carbon nitride (g-C3N4)-N-TiO2 heterojunction as an efficient
710 photocatalyst for the selective photoreduction of CO2 to CO. Applied Catalysis B: Environmental 158-
711 159, 20-29.
712 Zong, L., Zhang, J., Lu, G., Tang, Z., 2018. Controlled Synthesis of TiO2 Shape and Effect on the
713 Catalytic Performance for Selective Catalytic Reduction of NOx with NH3. Catalysis Surveys from
714 Asia 22, 105-117.

715